

Detection of noise correlations in two qubit systems by Machine Learning

Dario Fasone,^{1, 2, a)} Shreyasi Mukherjee,^{2, a)} Dario Penna,³ Fabio Cirinnà,³ Mauro Paternostro,⁴ Elisabetta Paladino,^{2, 5, 6} Luigi Giannelli,^{2, 5, b)} and Giuseppe A. Falci^{2, 5}

¹⁾*Dottorato di Ricerca in “Quantum Technologies”, Università di Napoli Federico II, Napoli, Italy*

²⁾*Dipartimento di Fisica e Astronomia “Ettore Majorana”, Università di Catania, Via S. Sofia 64, 95123 Catania, Italy*

³⁾*Leonardo S.p.A., Cyber & Security Solutions, 95121, Catania, Italy*

⁴⁾*Università degli Studi di Palermo, Dipartimento di Fisica e Chimica “Emilio Segrè”, via Archirafi 36, I-90123 Palermo, Italy*

⁵⁾*Istituto Nazionale di Fisica Nucleare, Sezione di Catania, 95123, Catania, Italy*

⁶⁾*CNR-IMM, UoS Università, 95123, Catania, Italy*

(Dated: 23 April 2026)

We introduce and validate a machine-learning assisted quantum sensing protocol to classify spatial and temporal correlations of classical noise affecting two ultrastrongly coupled qubits. We consider six distinct classes of Markovian and non-Markovian noise. Leveraging the sensitivity of a coherent population transfer protocol under three distinct driving conditions, the various forms of noise are discriminated by only measuring the final transfer efficiencies. Our approach achieves $\gtrsim 94\%$ accuracy in classification providing a near-perfect discrimination between Markovian and non-Markovian noise. The method requires minimal experimental resources, relying on a simple driving scheme providing three inputs to a shallow neural network with no need of measuring time-series data or real-time monitoring. The machine-learning data analysis acquires information from non-idealities of the coherent protocol highlighting how combining these techniques may significantly improve the characterization of quantum-hardware.

I. INTRODUCTION

Recently, accurate control of quantum systems has been achieved harnessing their inherent coherence to perform tasks in quantum communication and computation^{1, 2}. However, the loss of fidelity of quantum operations is still a problem mainly because of the interaction of the system with environmental degrees of freedom leading to decoherence³. Therefore, methods for noise diagnostics and strategies to mitigate its effects⁴ are paramount for the advancement of quantum technologies.

While for *single* qubits, optimized design has allowed to achieve protection from decoherence beyond the error-correction threshold^{5, 6}, substantial work has to be done in upscaled quantum architectures. In such contexts, coherence times are shorter and detrimental effects of time- and space-correlated noise may be significant. For example, in solid-state devices, impurities in the substrates are sources of non-Markovian⁷ and space-correlated noise⁸ that may also originate from shared control lines or collective electromagnetic modes. In recent experiments, space-correlated $1/f$ noise in superconducting and semiconducting spin qubits has been characterized^{9–13}. Similar correlations have been measured, long ago, in systems of small metallic tunnel junctions¹⁴. The characterization of noise correlations is thus a critical requirement for the

advancement of large-scale quantum computing, as standard protocols and quantum error correction (QEC) thresholds often assume negligible correlations between qubit errors. This assumption may not hold in upscaled quantum architectures¹⁵ and can require the development of new noise-mitigation strategies. A variety of spectroscopic and computational methods have been developed to detect and classify these environmental influences. Experimental efforts have largely focused on spectroscopic protocols to quantify spatial dependencies. In Ref.¹⁰ the authors utilized the coherence times of specific parallel and anti-parallel Bell states to distinguish between correlated and anti-correlated noise in Si/SiGe qubits. Building on this, interleaved Ramsey sequences and Bayesian estimation were implemented to reconstruct cross-power spectral densities^{12, 13}. To avoid the need for entangled-state preparation, Ref.⁹ introduced a two-qubit spectroscopy protocol based on continuous-control modulation (spin-locking), to simultaneously reconstruct all self- and cross-spectra. From a theoretical perspective, a framework to classify noise by its fundamental physical nature was developed¹¹, distinguishing between classical and quantum noise and two-qubit spectroscopy based on dynamical decoupling was addressed¹⁶.

Machine learning (ML) has recently established itself as a versatile technique that offers effective diagnostic and control tools for quantum hardware^{17–29}. ML-based techniques have been proposed for the classification of time-correlated noise in qubits, of energy-correlated fluctuations in qutrits³⁰ and networks³¹.

In this work, we propose a method for detecting and

^{a)}These authors contributed equally to this work.

^{b)}Corresponding author: luigi.giannelli@dfa.unict.it

classifying both temporal and spatial correlations of noise affecting a small Noise Intermediate Scale Quantum architecture³² by utilising minimal experimental resources. A driven two-qubit system is used as a sensor leveraging a control protocol inspired by Stimulated Raman Adiabatic Passage (STIRAP)^{33,34}. Implementations of this protocol in superconducting devices have been proposed^{35–38} and demonstrated^{39,40}. The design we study for sensing is well-suited to most superconducting-qubit, trapped-ion, and quantum-dot architectures.

While prior spectroscopic methods^{9,13} provide detailed spectral maps, they require significant experimental overhead and data processing. Similarly, existing ML approaches^{27–29,31} rely on measuring time-series data. In contrast, we propose a minimal data acquisition scheme consisting of simple measurements of STIRAP efficiency with three different combinations of drive amplitudes. Using synthetic data, we show that the resulting three-component feature vector is sufficient to train a multi-layer perceptron that reaches accuracies as high as 94% in discriminating both time- and space-correlations of noise. Markovianity of the quantum dynamics is almost perfectly discriminated, unveiling the ability of the method to extract information from the imperfections of the protocol.

This approach offers a framework that requires minimal experimental resources for the rapid characterisation of *global* properties of noise affecting quantum hardware. Furthermore, in contexts where a full noise estimation is needed, our approach could be a useful preliminary step. Once the nature of the spatial and time correlations of the noise is known, estimation protocols could be more efficiently tailored.

The paper is organized as follows. Section II introduces the two-qubit Hamiltonian and the stochastic noise models. In Sec. III, details of the control protocol and of the performance metrics are given. The machine-learning framework is described in Section IV, the results being presented and discussed in Section V. Finally, a summary and an outline of future perspectives are given in Sec. VI.

II. THE MODEL

A. The principal system

The sensor is modeled as a two-qubit system with energy splittings ϵ_i , for $i = 1, 2$, coupled by an Ising- xx interaction of strength g (see Fig. 1). The Hamiltonian reads ($\hbar = 1$)

$$H_S = -\frac{\epsilon_1}{2}\sigma_1^z - \frac{\epsilon_2}{2}\sigma_2^z + \frac{g}{2}\sigma_1^x\sigma_2^x, \quad (1)$$

σ_i^α for $\alpha = x, y, z$ being Pauli operators for the i -th qubit.

We denote with $|k\rangle$, for $k = 0, 1, 2, 3$, the eigenstates of H_S . Since the Hamiltonian conserves the parity $\Pi := \sigma_2^z\sigma_1^z$ of the number of excitations $N = (\sigma_1^z + \sigma_2^z)/2 +$

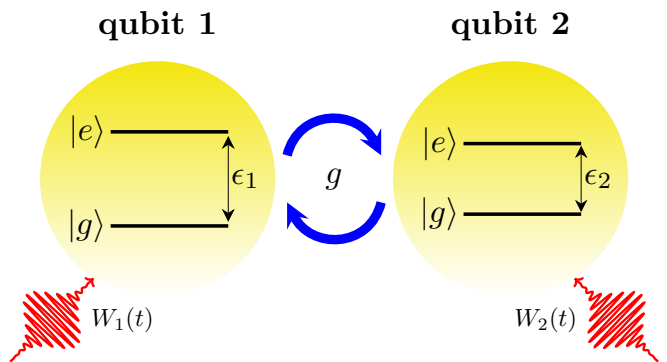


FIG. 1. Schematic representation of the sensor consisting of two qubits, with splittings ϵ_i , coupled with strength g and driven by external fields $W_i(t)$.

Subsp. Eigenv.	Eigenstate
\mathcal{H}_e	$-\epsilon_e$ $ 0\rangle \equiv -\cos\frac{\theta_e}{2} gg\rangle + \sin\frac{\theta_e}{2} ee\rangle$
	ϵ_e $ 1\rangle \equiv \sin\frac{\theta_e}{2} gg\rangle + \cos\frac{\theta_e}{2} ee\rangle$
\mathcal{H}_o	$-\epsilon_o$ $ 3\rangle \equiv -\cos\frac{\theta_o}{2} eg\rangle + \sin\frac{\theta_o}{2} ge\rangle$
	ϵ_o $ 2\rangle \equiv \sin\frac{\theta_o}{2} eg\rangle + \cos\frac{\theta_o}{2} ge\rangle$

TABLE I. Eigenvalues and eigenstates of the Hamiltonian (1). Here $\{|g\rangle, |e\rangle\}$ is the basis of each uncoupled qubit ($g = 0$) the mixing angles being defined as $\tan\theta_e = g/(\epsilon_1 + \epsilon_2)$ and $\tan\theta_o = g/(\epsilon_1 - \epsilon_2)$.

1, it admits two invariant subspaces, namely $\mathcal{H}_e := \text{span}\{|0\rangle, |1\rangle\}$ with even N and $\mathcal{H}_o := \text{span}\{|2\rangle, |3\rangle\}$ with odd N . The eigenenergies are respectively $\{-\epsilon_e, \epsilon_e\}$ and $\{-\epsilon_o, \epsilon_o\}$ with

$$\epsilon_e = \frac{1}{2}\sqrt{g^2 + (\epsilon_1 + \epsilon_2)^2} \quad ; \quad \epsilon_o = \frac{1}{2}\sqrt{g^2 + (\epsilon_1 - \epsilon_2)^2}.$$

The expressions of the eigenvectors are listed in Table I.

The system is operated by driving the two qubits locally, the control Hamiltonian

$$H_c(t) = \sum_i W_i(t) \sigma_i^x. \quad (2)$$

As drive changes the parity, $N \rightarrow N \pm 1$, the control Hamiltonian $H_c(t)$ is “off-diagonal” in the invariant subspace representation of table I (see App. A).

We now introduce a reference scenario where an ideal STIRAP can be operated. For the sake of simplicity, we take identical qubits $\epsilon_i = \epsilon$ so that the odd eigenstates are Bell states

$$\begin{aligned} |2\rangle &= \frac{1}{\sqrt{2}}(|ge\rangle + |eg\rangle), \\ |3\rangle &= \frac{1}{\sqrt{2}}(|ge\rangle - |eg\rangle), \end{aligned} \quad (3)$$

their energy splitting reduces to g . Then, if the system is driven symmetrically, $W_i(t) = W(t)$, a selection rule is

enforced, implying that the antisymmetric Bell state $|3\rangle$ is not coupled to the complementary subspace, $H_c|3\rangle = 0$. Thus, the driven dynamics is confined to a three-level system. As the drive doesn't commute with Π , it implements the so-called ladder configuration, shown in Fig. 6. We anticipate that non-ideal features emerging when lifting the above assumptions preserve or even improve the functionality of the noise sensor.

B. The control

To implement an ideal STIRAP, the control is operated by a two-tone field,

$$W(t) = \frac{1}{\beta} \Omega_s(t) \cos \omega_s t + \frac{1}{\alpha} \Omega_p(t) \cos \omega_p t, \quad (4)$$

where $\omega_p = \varepsilon + \frac{g}{2}$ is resonant with the $0 - 2$ transition and $\omega_s = \varepsilon - \frac{g}{2}$ with the $2 - 1$ transition, $\Omega_{p/s}(t)$ are slowly varying pulse envelopes, $\alpha = 2 \sin(\frac{\theta_\varepsilon}{2} - \frac{\pi}{4})$ and $\beta = 2 \sin(\frac{\theta_\varepsilon}{2} + \frac{\pi}{4})$. Here, we use Gaussian $\Omega_{p/s}(t)$ with width T (see App. A). The full Hamiltonian reads

$$H_S + H_c(t) = \varepsilon (|1\rangle\langle 1| - |0\rangle\langle 0|) + \frac{g}{2} (|2\rangle\langle 2| - |3\rangle\langle 3|) + W(t) (\alpha|0\rangle\langle 2| + \beta|2\rangle\langle 1| + \text{h.c.}), \quad (5)$$

To make explicit contact with STIRAP we introduce a doubly rotating frame and neglect terms of the drive oscillating at frequencies much larger than $\Omega_{p/s}$. In the new frame, the control Hamiltonian is approximated as (see App. A)

$$\tilde{H}_c(t) \approx \left[\frac{\Omega_p(t)}{\sqrt{2}} + \frac{\alpha}{\beta} \frac{\Omega_s(t)}{\sqrt{2}} e^{igt} \right] |0\rangle\langle 2| + \left[\frac{\Omega_s(t)}{\sqrt{2}} + \frac{\beta}{\alpha} \frac{\Omega_p(t)}{\sqrt{2}} e^{-igt} \right] |1\rangle\langle 2| + \text{h.c.} . \quad (6)$$

The standard Rotating Wave Approximation (RWA) is obtained by eliminating the terms that oscillate with frequency g , which would be accurate when $g \gg \Omega_{p/s}$. In this limit, the control Eq.6 implements the usual 3-level ‘‘ladder’’ configuration (see Fig. 2) admitting as an eigenvector a ‘‘dark state’’, i.e. a coherent superposition of $|0\rangle$ and $|1\rangle$. Its adiabatic dynamics (see Eq. (B4)) under a ‘‘counterintuitive’’ pulse sequence, where $\Omega_p(t)$ is delayed by a time τ with respect to $\Omega_s(t)$ (see Eq. (B3)), implements the ideal 3-level STIRAP protocol (see App. B), which results in coherent population transfer $|0\rangle \approx |gg\rangle \rightarrow |1\rangle \approx |ee\rangle$. During ideal STIRAP, the intermediate state $|2\rangle$ is never populated due to destructive interference. This scenario is also substantially valid under the action of the *full Hamiltonian* Eq (5), as shown in Fig. 3.

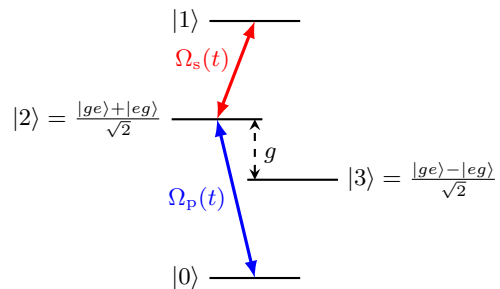


FIG. 2. Energy levels of the two-qubit sensor, for identical single-qubit splittings and symmetric driving. The highlighted transition implements a ladder driving configuration (see Eq. 6).

C. The Noise

We consider local noise affecting the level splittings of each qubit which is modeled by the Hamiltonian

$$H_n(t) = -\frac{1}{2} [\delta_1(t) \sigma_1^z + \delta_2(t) \sigma_2^z]. \quad (7)$$

where $\delta_i(t)$ for $i = 1, 2$ are classical stochastic processes⁴¹. This model accounts for the main mechanism degrading coherence during the adiabatic passage phase of population transfer^{33,34}, which is the heart of the quantum sensing protocol. Physically, it may arise in many cases, in particular by such as charge noise^{13,14,42}. Expressing $H_n(t)$ in the eigenbasis of H_S we obtain

$$H_n(t) = \frac{1}{2} (\delta_1 + \delta_2) \cos \theta_\varepsilon (|1\rangle\langle 1| - |0\rangle\langle 0|) + \frac{1}{2} \left[(\delta_1 - \delta_2) |3\rangle\langle 2| - \frac{g}{2\varepsilon} (\delta_1 + \delta_2) |0\rangle\langle 1| + \text{h.c.} \right]. \quad (8)$$

It is seen that noise induces nonideal features for STIRAP: (i) stochastic fluctuations to the energy splitting in the even subspace \mathcal{H}_e , which is the ‘‘trapped’’ subspace for STIRAP, and produce substantial dephasing; (ii) a coupling g between states $|2\rangle - |3\rangle$ inducing leakage from the two-level subspace; (i ii) a coupling between $|0\rangle - |1\rangle$. All these features are still compatible with STIRAP but produce a slightly different output (see Fig. 3, solid lines) providing information on the noise. For the data-analysis we consider six classes of noise, according to their time and space correlations:

- **Time-correlated (non-Markovian) noise:** In this context we address specifically the case of *quasistatic noise*, where the correlation time is larger than the duration of a single run of the protocol. Noise is reduced to random variables $\delta_i(t)$ constant during a single run, but varying for different runs. This is the leading effect of $1/f$ noise^{42–45} in solid-state quantum architectures. The values of $\delta_i(t)$ are picked from a Gaussian distribution

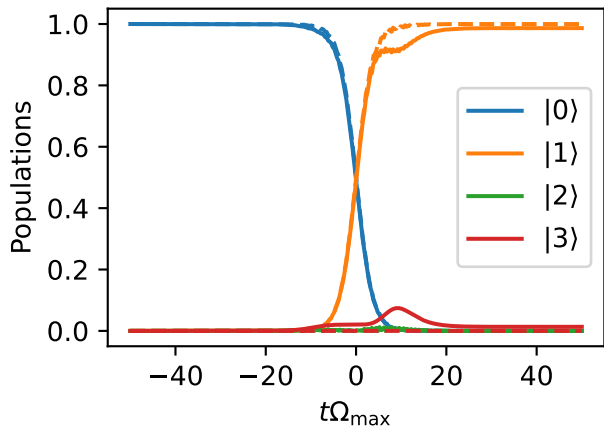


FIG. 3. Population histories of a system of two ultrastrongly coupled qubits, $g = 0.6\epsilon$. The dashed lines represent the dynamics with the full Hamiltonian Eq. (5). Pulses given by Eq. (B3) with parameters $\Omega_{p/s}^{\max} = \Omega_{\max} = 0.05\epsilon$, $\epsilon T = 2000$ and $\tau = 0.7T$. The evolution is close to ideal STIRAP. Quasistatic noise introduces imperfections (solid lines). Here $\delta_1 = 0.002\epsilon$ and $\delta_2 = -0.002\epsilon$.

with zero mean and standard deviation $\sigma = 10^{-2}\epsilon = 0.2\sqrt{(\Omega_p^{\max})^2 + (\Omega_s^{\max})^2}/2$, and describe the cumulative effects of many independent microscopic sources which are weakly individually coupled⁴⁴. Concerning space correlations we focus on three distinct classes:

- (1) Correlated: $\delta_2(t) = \eta\delta_1(t)$ with $\eta > 0$;
- (2) Anti-correlated: $\delta_2(t) = \eta\delta_1(t)$ with $\eta < 0$;
- (3) Uncorrelated: independent $\delta_2(t)$ and $\delta_1(t)$.

- **Markovian noise:** We consider zero-mean $\langle\delta_i(t)\rangle = 0$, delta-correlated $\langle\delta_i(t)\delta_i(t')\rangle = \gamma\delta(t-t')$ stochastic processes, thus the dynamics of the two-qubits is described by a Markovian map and does not depend on its history. Here we consider again three instances of space-correlations:

- (4) Correlated: $\delta_2(t) = \eta\delta_1(t)$, with $\eta > 0$;
- (5) Anti-correlated: $\delta_2(t) = \eta\delta_1(t)$, with $\eta < 0$.
- (6) Uncorrelated: independent $\delta_2(t)$ and $\delta_1(t)$.

While real hardware noise may exhibit more complex spectral features, non-Gaussian statistics, or additional couplings, the aim of the present work is not to reproduce a specific experimental device. Rather, we focus on demonstrating that global properties of noise correlations—both temporal and spatial—can be reliably discriminated using minimal experimental information. The proposed framework is general and can be straightforwardly extended to incorporate other types or platform-specific noise models.

III. POPULATION TRANSFER IN THE NOISE SENSOR

Our main goal is to classify the different noises by Machine Learning, using the efficiency of a STIRAP-like protocol, as a fingerprint. The full Hamiltonian describing the driven dynamics of the sensor in the presence of noise is given by $H_S + H_c(t) + H_n(t)$. The main effect of noise (as described in Sec. II) is due to the diagonal entries of $H_n(t)$ in the eigenbasis of H_S , see eq. (8), since the dark state is not anymore an eigenstate of the full (dressed) Hamiltonian. As a consequence, adiabatic patterns do not lead to population transfer. However, for small enough $\delta_i \ll \Omega_{p/s}^{\max}$ almost complete population transfer occurs via diabatic transitions. In addition, noise may also couple the antisym metric Bell state $|3\rangle$ with $|2\rangle$, the dynamics now involving the whole 4-level Hilbert space. Remarkably, $|3\rangle$ gets populated during time evolution even if the noise is small $\delta_1, \delta_2 \ll \epsilon$. An example of population histories in the four-level system is shown in Fig. 3 (solid lines).

A. Efficiency

In the foregoing we will study the efficiency of the protocol defined as the final population of the state $|ee\rangle$, that is

$$\xi = \lim_{N \rightarrow \infty} \frac{1}{N} \sum_{r=1}^N \xi^{(r)} \quad (9)$$

where $\xi^{(r)} = \langle ee | \rho_f^{(r)} | ee \rangle$ and $\rho_f^{(r)}$ is the density matrix of the system at the final time t_f for the r -th noise realization. This is not the usual efficiency of STIRAP given by the final population of the target state $|1\rangle$ which is entangled, measurements in the local basis providing a simpler data-acquisition scheme. For quasistatic noise, which remains constant during the individual trajectory, the index r can be uniquely associated with the two real values $\delta_1^{(r)}$ and $\delta_2^{(r)}$, which are specific values of the random variables δ_1 and δ_2 , respectively. Therefore we write $\xi^{(r)} = \xi(\delta_1^{(r)}, \delta_2^{(r)})$ and express the efficiency Eq. (9) via the joint probability distribution $p(\delta_1, \delta_2)$

$$\xi = \int d\delta_1 d\delta_2 \xi(\delta_1, \delta_2) p(\delta_1, \delta_2). \quad (10)$$

The efficiency for equal peak values of the drives, $\Omega_s^{\max} = \Omega_p^{\max}$, is reported in Fig. 4 as a function of the values of the quasistatic noises δ_i . We emphasize that our goal is not to achieve efficient population transfer, but rather to leverage the protocol's sensitivity to extract information about noise, which reduces the efficiency. Fig. 4 suggests that the average efficiency strongly depends on the correlations of the random variables δ_i . This information will be accessed by considering three different ratios $\Omega_s^{\max}/\Omega_p^{\max}$ of the peak pulse amplitudes (see Fig. 7). For

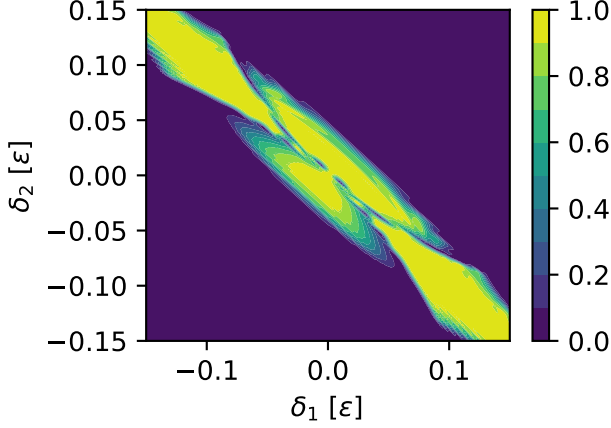


FIG. 4. Efficiency of the STIRAP-like protocol versus the quasistatic noises δ_1 and δ_2 for equal peak amplitudes $\Omega_{p/s}^{\max}$. The parameters are the same as in Fig. 3.

perfectly correlated or anti-correlated noise, $\delta_2^{(r)} = \eta \delta_1^{(r)}$, Eq. (10) simplifies

$$\xi = \int d\delta_1 \xi(\delta_1, \eta\delta_1) p(\delta_1). \quad (11)$$

For uncorrelated noises the joint probability factorizes. For Markovian noise, the efficiency is obtained by solving a Lindblad master equation (see Appendix. C)

$$\begin{aligned} \langle \dot{\rho}(t) \rangle = & -i[H(t), \rho(t)] + \\ & + \sum_k \gamma_k \left(O_k^\dagger \rho(t) O_k - \frac{1}{2} [O_k^\dagger O_k, \rho(t)]_+ \right), \end{aligned} \quad (12)$$

where $\langle \cdot \rangle$ denotes the average over the stochastic process. Uncorrelated noise is described by two jump operators which in the eigenbasis of H_S read

$$\begin{aligned} O_1 = & \frac{1}{2} \left[\cos \theta_e (|1\rangle\langle 1| - |0\rangle\langle 0|) + (|2\rangle\langle 3| + |3\rangle\langle 2|) + \right. \\ & \left. \frac{g}{2\varepsilon} |0\rangle\langle 1| + h.c \right] \\ O_2 = & \frac{1}{2} \left[\cos \theta_e (|1\rangle\langle 1| - |0\rangle\langle 0|) - (|2\rangle\langle 3| + |3\rangle\langle 2|) + \right. \\ & \left. \frac{g}{2\varepsilon} |0\rangle\langle 1| + h.c \right] \end{aligned} \quad (13)$$

A single jump operator describes instead correlated/anticorrelated noise

$$\begin{aligned} O = & \frac{1}{2} \left[\left(\frac{1+\eta}{\sqrt{|\eta|}} \cos \theta_e \right) (|1\rangle\langle 1| - |0\rangle\langle 0|) + \right. \\ & - \left(\frac{g}{2\varepsilon} \frac{1+\eta}{\sqrt{|\eta|}} \right) (|0\rangle\langle 1| + |1\rangle\langle 0|) \\ & \left. + \left(\frac{1-\eta}{\sqrt{|\eta|}} \right) (|2\rangle\langle 3| + |3\rangle\langle 2|) \right]. \end{aligned} \quad (14)$$

IV. MACHINE LEARNING MODEL AND DATA GENERATION

A. ML model

We employ a neural network (NN), namely a Multi Layer Perceptron (MLP), to perform supervised learning^{46,47} and classify the type of noise affecting the two-qubit system. A NN is a parameterized function capable of approximating a broad class of target functions⁴⁸; the specific architecture we use is reported in Table II.

Layer	# Neurons	Activation Function
Input	3	
Hidden 1	64	ReLU
Hidden 2	32	ReLU
Hidden 3	32	LeakyReLU
Hidden 3	32	LeakyReLU
Output	6	Softmax

TABLE II. Layout of the neural network for classifying the types of noise.

Supervised learning consists in fitting a function approximator (in this case, the NN) that maps inputs to outputs by minimizing a cost function over a labeled dataset. This procedure is referred to as *training* the neural network^{17,46}. The dataset consists of input-output pairs $(\mathbf{x}_i, \hat{\mathbf{y}}_i)_{i=1,2,\dots,N}$, where each input \mathbf{x}_i is associated with a corresponding output $\hat{\mathbf{y}}_i$, also called label. Here the label $\hat{\mathbf{y}}_i$ for each sample i is an integer $a = 0, 1, 2, 3, 4, 5$ representing one of the noise classes described in Sec. II C. The output \mathbf{y}_i of the NN is a 6 dimensional real vector whose components $y_{i,j}$ represent the probabilities that the noise affecting the system of sample i is of class j . The use of the *Softmax*^{46,49} activation in the output layer (see Tab. II) ensures that the model outputs form a normalized probability distribution. We minimize the *sparse categorical cross-entropy*⁵⁰ cost function

$$C = -\frac{1}{N} \sum_{i=1}^N \log(y_{i,\hat{\mathbf{y}}_i}), \quad (15)$$

which is well-suited for multi-class classification tasks.

This choice encourages the model to assign high probability to the correct label. The training process is monitored through the classification accuracy, defined as

$$A = \frac{1}{N} \sum_{i=1}^N \delta(\arg \max_j y_{i,j}, \hat{\mathbf{y}}_i), \quad (16)$$

where δ is the Kronecker delta, and $\arg \max_j$ returns the

index j of the largest component of the corresponding vector.

More details on the neural network architecture and training procedure are provided in the Appendix D.

B. Data generation

We use as input to the ML model the STIRAP efficiencies measured under three different driving conditions³⁰

- (i) $\Omega_p^{\max} = \Omega_s^{\max}$,
- (ii) $\Omega_p^{\max} = 2\Omega_s^{\max}$,
- (iii) $\Omega_p^{\max} = \Omega_s^{\max}/2$,

with the constraint $(\Omega_p^{\max})^2 + (\Omega_s^{\max})^2$ constant. This approach is advantageous as it provides high sensitivity to noise while requiring low experimental effort and is straightforward to implement in most physical systems. In fact the measurement has to be performed only at the end of (and not during) the evolution. This eliminates the necessity for time series data and may drastically reduce the duration of the experiment. In fact, by relying exclusively on final-state populations, the protocol avoids time-resolved measurements or continuous monitoring. This substantially reduces experimental overhead, data acquisition and storage requirements, and makes the approach particularly suitable for scalable implementations.

To generate the dataset, we numerically simulate the dynamics of the two-qubits system and evaluate the efficiency as reported in Sec. III A. Each input data point is then a three dimensional Real vector $\mathbf{x} = (\xi_{\Omega_p=\Omega_s}, \xi_{\Omega_p>\Omega_s}, \xi_{\Omega_p<\Omega_s})$.

For correlated (anti-correlated) non-Markovian noise we generate each data sample by randomly selecting the correlation parameter η within the range $[0.1, 5]$ ($[-5, -0.1]$). For each choice of η , we numerically evaluate the efficiency, eq. (11), under the three pulse conditions outlined earlier, yielding a single sample.

For uncorrelated non-Markovian noise instead, as the two random variables δ_1 and δ_2 are independent, we vary the standard deviation of the Gaussian distributions $p_1(\delta_1)$ and $p_2(\delta_2)$ respectively within the range $\sigma_1, \sigma_2 \in [\frac{\sigma}{5}, 5\sigma]$, with $\sigma = 10^{-2}\epsilon$ before calculating every data sample. We then numerically calculate the efficiencies under the three pulse condition using eq. (10).

In the context of Markovian, correlated (anti-correlated) noise, the efficiencies are calculated numerically solving the Lindblad master equation, eq. 12. In this particular instance, not only does η fluctuate within the specified ranges, like correlated (anti-correlated) non-Markovian scenarios from one sample to another, but also we randomly select the decay parameter $\gamma \in [10^{-4}, 10^{-3}]\epsilon$. Whereas, for uncorrelated Markovian noise we randomly select the

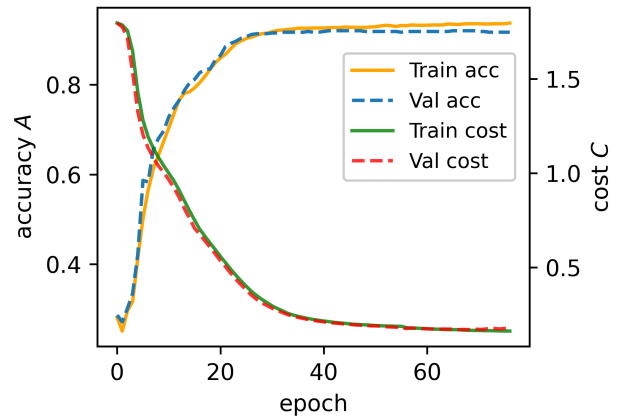


FIG. 5. Accuracy (16) and value of the cost function, Eq. (15), for the training (solid lines) and validation (dashed lines) sets versus the number of epochs of training. The accuracy on the test set is $A \approx 94\%$.

decay parameters $\gamma_1, \gamma_2 \in [10^{-4}, 10^{-3}]\epsilon$. For each noise class, we generate 500 samples. The total dataset is split into a 3 : 1 : 1 ratio for training, validation, and test set respectively.

V. RESULTS

We train the NN model described in Tab. II. The output \mathbf{y}_i of the neural network for a given input vector \mathbf{x}_i , denoted as is compared to the corresponding true label $\hat{\mathbf{y}}_i$. The training progress of the model is illustrated in Fig. 5, where panel (a) shows the classification accuracy A , eq. 16. The accuracy increases with the number of training epochs. Panel (b) shows that the cost function C , eq. 15, decreases accordingly. After about 70 training epochs, the model achieves a classification accuracy of $(94 \pm 2)\%$, the variation being due to the random initialization of model parameters, as well as the stochastic shuffling and splitting of the dataset. The classification performance of the model is further analyzed using the confusion matrix in Fig. 6, which compares the true noise classes with the predicted ones. Each row corresponds to a true noise class, while each column represents the predicted class. The six diagonal elements indicate the percentage of correct predictions for each noise class. The model achieves an accuracy of 99% in distinguishing between non-Markovian and Markovian noise. It correctly classifies space correlations of non-Markovian noise with an accuracy of 97.3%, whereas within the Markovian class, the classification accuracy is 91.7%.

Insight on how non-Markovian noise is classified is provided by Fig. 7 where the efficiency vs the realizations (δ_1, δ_2) of quasistatic noise is reported for different ratios $\Omega_s^{\max}/\Omega_p^{\max}$ of the peak amplitudes of the drives. Non-

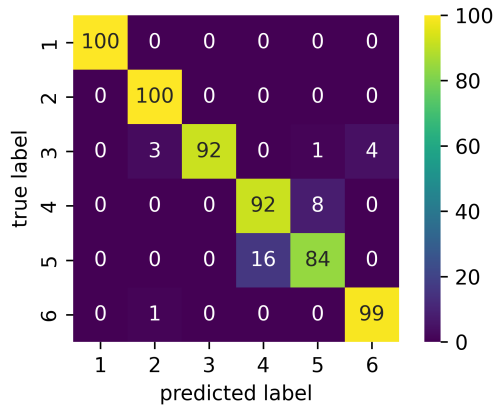


FIG. 6. . Confusion matrix of the MLP model for classifying the noise types described in Sec. II C. Each row represents the true noise class, while each column corresponds to the predicted class. The classification reaches an accuracy of $\approx 94\%$

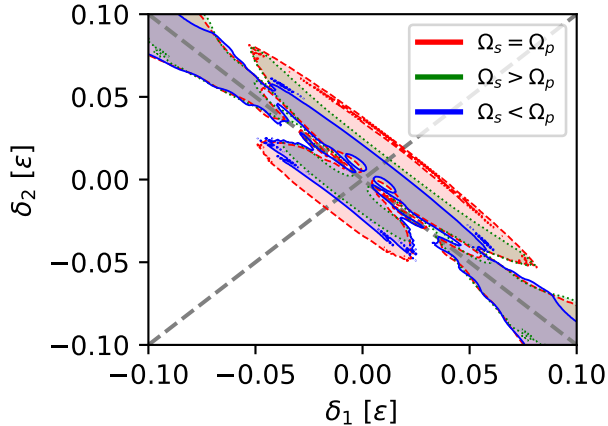


FIG. 7. Contour plot of the efficiency of the STIRAP-like protocol. The lines enclosing the different regions correspond to 75% efficiency of population transfer for different ratios between the peak values of the pulse amplitudes. The parameters are the same of fig. 4. The dashed lines $\delta_1 = \pm\delta_2$ emphasize the different statistics of correlated and anticorrelated quasistatic noise.

Markovian quasistatic noises randomly shift the energy splitting of the corresponding qubit at each repetition of the protocol. Consequently, for fully correlated (anticorrelated) quasistatic noise, the overall efficiency is obtained as the weighted integral of the single trajectory efficiency over a line $\delta_2 = \eta\delta_1$, see eq. (11). Since the efficiency profiles depend on the driving conditions and are different for $\eta > 0$ or $\eta < 0$, also the average efficiencies are expected to depend on driving conditions and correlations. Even if it is not immediate that this may lead to efficient discrimination, data analysis by ML

provides a robust solution to this problem.

For uncorrelated quasistatic noise, where the weighted integral is over the whole $\delta_1 - \delta_2$ plane (see eq. (10)), the situation is less clear. For Markovian noise the efficiency for each trajectory cannot be represented as a single point (δ_1, δ_2) and the analysis is even more involved. Yet discrimination by ML is to a large extent successful.

We notice that, compared to an earlier work on correlated noise in three-level systems³⁰, where ML was unable to detect energy correlations between different Markovian noises, the two-qubit setup allows to discriminate space correlations of Markovian noise. This enhanced classification ability stems from the noise-induced mixing of the intermediate states $|2\rangle - |3\rangle$ and $|0\rangle - |1\rangle$ (see Eq. (8)). As a consequence, the dynamics involves the whole 4-level Hilbert space to an extent *depending on the correlations* which makes the discrimination effective also for Markovian noise.

Figure 8 reports the noise classification accuracy A , eq. (16) as a function of the qubit-qubit coupling strength g . For each value of g we generated a labeled dataset of 3000 samples, tuned the neural network architecture, and trained the model to evaluate the corresponding classification accuracy. For $g \geq 0.2\epsilon$, the accuracy

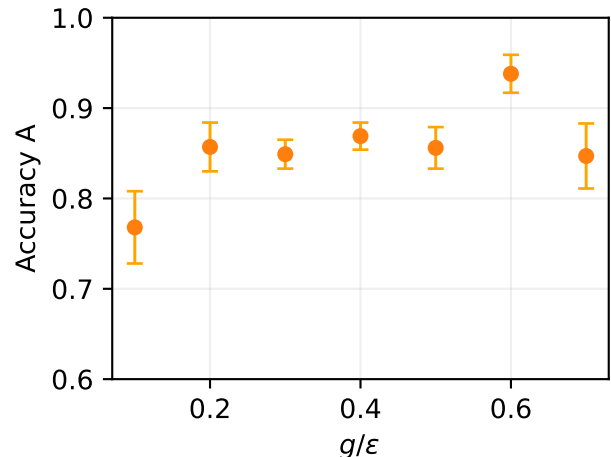


FIG. 8. Accuracy A vs the qubit-qubit coupling strength g . Other parameters are reported in Sec. IV B. The error is estimated as the semi-dispersion over 10 independent training runs per dataset, with randomized parameter initialization and data splitting.

always remains higher than 80%, demonstrating the robustness of the protocol versus different values of g . The maximum accuracy obtained is $A \approx 0.94$ and is reached at $g = 0.6\epsilon$.

VI. CONCLUSIONS

In this work, we have proposed and numerically validated a machine learning-assisted quantum sensing

which categorizes classical noises affecting a two-qubit system. The protocol extracts global information on time and/or space correlations of noise. We defined and successfully classified six distinct noise classes, namely correlated/anti-correlated/uncorrelated non-Markovian and Markovian noises. Our approach leverages the sensitivity of coherent population transfer by a non-ideal STIRAP-like protocol to the amplitudes of the drives. Variations in the efficiency provide a fingerprint of the underlying noise correlations.

By measuring only the final population of the doubly excited state $|ee\rangle$ under the three distinct driving conditions, the protocol achieves a classification accuracy higher than 80% for several values of the qubit-qubit coupling strength g , with a peak of $A \approx 94\%$ at $g = 0.6\epsilon$. Furthermore, discrimination of time-correlations is nearly perfect. Remarkably, this approach requires only three inputs to a shallow neural network, with no need for time-series data or real-time monitoring and requires a simple driving scheme, thus having a minimal experimental overhead. This approach of noise classification and characterization differs from standard methods such as reconstruction of noise power spectra or full process tomography. While these techniques provide more detailed information about the environment, they require much more time and experimental resources. In contrast, our method quickly extracts global properties of the noise using only a small number of measurements.

Several driving control schemes have been found^{33,34,51-53} which can be employed in different implementations of the sensor. Data can in principle be collected by averaging single-shot measurements of each qubit. An experimentally less demanding procedure is a continuous measurement⁵⁴ of the decay of each atom into a transmission line. A large signal is obtained if such decay is faster than the individual atomic non-radiative decay⁵⁵. In the simplest instance, the transmission line is coupled to the mode during the whole protocol. As analyzed in Ref. 56, despite the apparent invasivity, the measurement backaction is expected to have little effect on STIRAP, since the main effect is the decay of the final state when populated, which is the measurement itself.

Differently from the previous work on correlated noise in three-level systems³⁰, the two-qubit setup allows to discriminate space correlations of Markovian noise. This enhanced sensitivity arises from the richer physics of the four-level system, where noise may induce deviations from the ideal protocol. These latter provide qualitatively new data which improve the discrimination power of the supervised learning analysis.

The main goal of this work is to demonstrate the feasibility of detecting noise correlations using a small set of features obtained from an advanced quantum control protocol, and analyzed by supervised learning. Future work will broaden the scope of our approach to achieve a finer classification of correlations by exploiting other non-idealities of the protocol, by

utilizing alternative control schemes, and by identifying additional input features. Simultaneous optimization of parameters of the sensor besides the coupling g , such as the STIRAP parameters $\Omega_{p/s}^{\max}$ and τ , could further improve the accuracy. Furthermore, the size of the sensor can be increased by considering array of qubits which may provide richer noise fingerprints: collective phenomena in these multi-qubits systems are also expected to provide an advantage in achieve a finer classification. Another important step would be tailoring unsupervised learning strategies for noise classification. We believe that the synergy between coherent control schemes and ML approaches, by further enhancing classification sensitivity and broadening applicability to diverse quantum platforms, will play a key role in the next-generation quantum-hardware diagnostics.

Appendix A: Control Hamiltonian

The control Hamiltonian Eq.(2) describes local drives acting on each qubit. In the basis of the eigenstates of H_S it reads

$$\begin{aligned} H_c(t) = & - [W_1 \sin(\frac{\theta_o - \theta_\epsilon}{2}) + W_2 \cos(\frac{\theta_o + \theta_\epsilon}{2})] |0\rangle\langle 2| + \\ & + [W_1 \cos(\frac{\theta_o - \theta_\epsilon}{2}) + W_2 \sin(\frac{\theta_o + \theta_\epsilon}{2})] |1\rangle\langle 2| + \\ & + [W_1 \cos(\frac{\theta_o - \theta_\epsilon}{2}) - W_2 \sin(\frac{\theta_o + \theta_\epsilon}{2})] |0\rangle\langle 3| + \\ & + [W_1 \sin(\frac{\theta_o - \theta_\epsilon}{2}) - W_2 \cos(\frac{\theta_o + \theta_\epsilon}{2})] |1\rangle\langle 3| + h.c. \end{aligned} \quad (A1)$$

resulting “off-diagonal” in the invariant subspace representation (table I) since operators σ_i^x in the drive change the parity. From Eq. A1, we identify under which either state $|2\rangle$ or $|3\rangle$ are decoupled in the dynamics. This happens when $\theta_o = \pi/2$ and $\frac{W_1}{W_2} = \pm 1$, where the positive sign applies to state $|3\rangle$, and the negative sign applies to $|2\rangle$.

For symmetric driving, $W_1 = W_2 = W$, the above equation simplifies

$$\begin{aligned} H_c(t) = & 2W(t) [\sin(\frac{\theta_o}{2} + \frac{\pi}{4}) \sin(\frac{\theta_\epsilon}{2} - \frac{\pi}{4}) |0\rangle\langle 2| + \\ & + \sin(\frac{\theta_o}{2} + \frac{\pi}{4}) \sin(\frac{\theta_\epsilon}{2} + \frac{\pi}{4}) |1\rangle\langle 2| + \\ & + \sin(\frac{\theta_o}{2} - \frac{\pi}{4}) \sin(\frac{\theta_\epsilon}{2} - \frac{\pi}{4}) |0\rangle\langle 3| + \\ & + \sin(\frac{\theta_o}{2} - \frac{\pi}{4}) \sin(\frac{\theta_\epsilon}{2} + \frac{\pi}{4}) |1\rangle\langle 3| + h.c.], \end{aligned} \quad (A2)$$

and condition $\theta_o = \frac{\pi}{2}$ is found, corresponding to identical qubits, $\epsilon_i =: \epsilon$.

The unitary transformation to the doubly rotating frame used to derive Eq. 6 is given by

$$U_x(t) = e^{-i(\omega_s + \omega_p)t} |1\rangle\langle 1| + e^{-i\omega_p t} |2\rangle\langle 2|. \quad (A3)$$

The frequencies of the drives are taken as

$$\omega_p = \epsilon + \frac{g}{2} - \Delta_p, \quad (A4a)$$

$$\omega_s = \epsilon - \frac{g}{2} - \Delta_s. \quad (A4b)$$

where Δ_s and Δ_p are the detunings. Denoting with $H(t)$ the full Hamiltonian Eq. 5 and transforming to the rotating frame, $\tilde{H}(t) = U_x(t)^\dagger H(t) U_x(t) - i U_x(t)^\dagger \partial_t U_x(t)$, we obtain

$$\begin{aligned} \tilde{H}(t) = & (\Delta_p + \Delta_s) |1\rangle\langle 1| + \Delta_p |2\rangle\langle 2| + \left(\varepsilon + \frac{g}{2}\right) |3\rangle\langle 3| + \\ & + \left\{ \alpha \left[\frac{\Omega_p}{\sqrt{2}\alpha} (e^{-2i\omega_p t} + 1) + \frac{\Omega_s}{\sqrt{2}\beta} (e^{i\omega_- t} + e^{-i\omega_+ t}) \right] |0\rangle\langle 2| + \right. \\ & + \beta \left[\frac{\Omega_s}{\sqrt{2}\beta} (e^{-2i\omega_s t} + 1) + \frac{\Omega_p}{\sqrt{2}\alpha} (e^{-i\omega_- t} + e^{-i\omega_+ t}) \right] |2\rangle\langle 1| \\ & \left. + h.c. \right\}, \quad (\text{A5}) \end{aligned}$$

where $\omega_- = \omega_s - \omega_p$ and $\omega_+ = \omega_s + \omega_p$. Since $2\omega_s, 2\omega_p, \omega_+ \gg \omega_s, \omega_p$ we can neglect fastly oscillating terms⁵⁷, obtaining

$$\begin{aligned} \tilde{H}(t) = & \Delta_p |2\rangle\langle 2| + (\Delta_p + \Delta_s) |1\rangle\langle 1| + \left(\varepsilon + \frac{g}{2}\right) |3\rangle\langle 3| + \\ & + \left\{ \alpha \left[\frac{\Omega_p}{\sqrt{2}\alpha} + \frac{\Omega_s}{\sqrt{2}\beta} e^{i(\Delta_s - \Delta_p - g)t} \right] |0\rangle\langle 2| + \right. \\ & \left. + \beta \left[\frac{\Omega_s}{\sqrt{2}\beta} + \frac{\Omega_p}{\sqrt{2}\alpha} e^{-i(\Delta_s - \Delta_p - g)t} \right] |2\rangle\langle 1| + h.c. \right\}, \quad (\text{A6}) \end{aligned}$$

If both the drives are resonant $\Delta_p = \Delta_s = 0$ we obtain the Hamiltonian eq. (6) presenting a time-dependent term oscillating at a frequency g .

Appendix B: STIRAP

STIRAP^{33,34} is a protocol yielding efficient and robust population transfer in a three-level system. We design our system such as STIRAP is operated in $\text{span}\{|0\rangle, |2\rangle, |1\rangle\}$ (see Fig. 2). The system is driven by two time-dependent classical fields: the *pump pulse* $\Omega_p(t)$ drives the transition $|0\rangle - |2\rangle$, while the *Stokes pulse* drives the transition $|2\rangle - |1\rangle$. The Hamiltonian in an appropriate rotating frame reads²¹

$$\begin{aligned} H_S(t) = & \Delta |1\rangle\langle 1| + \Delta_p |2\rangle\langle 2| + \\ & + \frac{1}{2} (\Omega_p(t) |0\rangle\langle 2| + \Omega_s(t) |2\rangle\langle 1| + h.c.), \quad (\text{B1}) \end{aligned}$$

where $\Delta_p = \varepsilon + \frac{g}{2} - \omega_p$ and $\Delta = 2\varepsilon - \omega_p - \omega_s$ are the single and two-photon detunings, respectively, and ω_p and ω_s are the frequencies of the pump and Stokes fields, respectively. For efficient population transfer, it is crucial to operate at small two-photon detuning, $\Delta \ll \Omega_{p,s}$. In particular, under two-photon resonance ($\Delta = 0$), H_S admits the so-called ‘‘dark state’’ as an instantaneous eigenstate

$$|\phi_D\rangle = \cos \theta(t) |0\rangle - \sin \theta(t) |1\rangle, \quad (\text{B2})$$

with $\tan \theta(t) = \Omega_p(t)/\Omega_s(t)$. If the pulses are shined in a *counterintuitive sequence*, i.e., Ω_s is applied before Ω_p , while ensuring that they overlap for part of the protocol,

then $\theta(t)$ smoothly varies from 0 to $\pi/2$. When the system is initialized in the state $|\phi_D(t_i)\rangle = |0\rangle$, if the evolution remains adiabatic^{58,59} the system will follow the dark state $|\phi_D\rangle$ reaching the desired target state at the final time $|\phi_D(t_f)\rangle = |1\rangle$.

It is well known that STIRAP is robust against variations in the pulse shapes³⁴. Among the many possible choices⁶⁰, in this work, we use Gaussian pulses, given by

$$\Omega_p(t) = \Omega_p^{\max} e^{-\left(\frac{t-\tau}{T}\right)^2}, \quad \Omega_s(t) = \Omega_s^{\max} e^{-\left(\frac{t+\tau}{T}\right)^2}, \quad (\text{B3})$$

and evolve the system over the time interval $[-5T, 5T]$, with $\tau = 0.7T$. Adiabaticity is ensured by the global condition³³

$$\Omega_{p/s}^{\max} \tau \geq 10. \quad (\text{B4})$$

The efficiency of the protocol is defined as the population of the target state $|1\rangle$ at the end of the evolution. The formal definition is given directly in Sec. III A for the system of interest.

Appendix C: Derivation of the Master Equation for Markovian noise

In this section we outline the derivation of the Master Equation for Markovian (anti)correlated noise. The system Hamiltonian is defined by eq. 5, while the effect of the noise is described by eq. 7, with $\delta_1 = \frac{1}{\sqrt{\eta}}\chi$ and $\delta_2 = \sqrt{\eta}\chi$, obtaining:

$$H_n = \chi(t)O, \quad (\text{C1})$$

with

$$\begin{aligned} O = & \frac{1}{2} \left[\left(\frac{1+\eta}{\sqrt{|\eta|}} \cos \theta_e \right) (|1\rangle\langle 1| - |0\rangle\langle 0|) + \right. \\ & - \left(\frac{g}{2\varepsilon} \frac{1+\eta}{\sqrt{|\eta|}} \right) (|0\rangle\langle 1| + |1\rangle\langle 0|) \\ & \left. + \left(\frac{1-\eta}{\sqrt{|\eta|}} \right) (|2\rangle\langle 3| + |3\rangle\langle 2|) \right]. \quad (\text{C2}) \end{aligned}$$

We consider noise with zero mean, $\langle \chi(t) \rangle = 0$, and Markovian $\langle \chi(t)\chi(t') \rangle = \gamma \delta(t-t')$. The density matrix $\tilde{\rho}(t)$ in the interaction picture solves the von Neumann equation $\dot{\tilde{\rho}}(t) = -i [\tilde{H}_n, \tilde{\rho}(t)]$ which can be formally integrated and averaged over the stochastic process yielding

$$\langle \dot{\tilde{\rho}}(t) \rangle = - \left\langle \int_0^t [\chi(t)\tilde{O}(t), [\chi(t')\tilde{O}(t'), \tilde{\rho}(t')]] dt' \right\rangle, \quad (\text{C3})$$

For Markovian noise, we can write $\langle \chi(t)\chi(t')\tilde{\rho}(t') \rangle = \langle \chi(t)\chi(t') \rangle \tilde{\rho}(t')$, since $t' < t$, and $\tilde{\rho}(t')$ cannot depend

on t , except for $t' = t$, obtaining

$$\langle \dot{\rho}(t) \rangle = \gamma \left(\tilde{O}^\dagger(t) \tilde{\rho}(t) \tilde{O}(t) - \frac{1}{2} [\tilde{O}^\dagger(t) \tilde{O}(t), \tilde{\rho}(t)]_+ \right) \quad (\text{C4})$$

which in the Schrödinger picture reads

$$\langle \dot{\rho}(t) \rangle = -i [H(t), \rho(t)] + \gamma \left(O^\dagger \rho(t) O - \frac{1}{2} [O^\dagger O, \rho(t)]_+ \right) \quad (\text{C5})$$

For zero mean, uncorrelated Markovian local noises, the noise Hamiltonian is

$$H_n(t) = \sum_{k=1,2} \delta_k(t) O_k, \quad (\text{C6})$$

the two collapse operators being

$$O_1 = \frac{1}{2} [\cos \theta_e (|1\rangle\langle 1| - |0\rangle\langle 0|) + (|2\rangle\langle 3| + |3\rangle\langle 2|) + \frac{g}{2\varepsilon} |0\rangle\langle 1| + h.c], \quad (\text{C7})$$

$$O_2 = \frac{1}{2} [\cos \theta_e (|1\rangle\langle 1| - |0\rangle\langle 0|) - (|2\rangle\langle 3| + |3\rangle\langle 2|) + \frac{g}{2\varepsilon} |0\rangle\langle 1| + h.c]. \quad (\text{C8})$$

Repeating the same steps as before, and using the relation

$$\langle \delta_k(t) \delta_l(t') \rangle = \gamma_k \delta_{kl} \delta(t - t'); \quad k, l = 1, 2, \quad (\text{C9})$$

cross terms vanish and in the Schrödinger picture we obtain

$$\langle \dot{\rho}(t) \rangle = -i [H(t), \rho(t)] + \sum_k \gamma_k \left(O_k^\dagger \rho(t) O_k - \frac{1}{2} [O_k^\dagger O_k, \rho(t)]_+ \right). \quad (\text{C10})$$

Appendix D: Neural Networks

Neural networks (NNs)^{46,47} are at the heart of modern artificial intelligence and have become essential in a wide range of applications, including computer vision, speech recognition, natural language processing, and autonomous systems. These models excel at capturing complex, non-linear patterns in data, enabling machines to perform classification, regression, and decision-making tasks with impressive accuracy. Inspired by the structure of the human brain, neural networks are composed of layers of interconnected artificial neurons that learn representations from data through iterative optimization techniques. Their flexibility, adaptability, and scalability make them indispensable in both theoretical research and real-world engineering solutions across diverse domains.

A NN is a function⁶¹

$$\text{NN}_{\Theta}(\mathbf{x}) : \mathbf{x} \rightarrow \mathbf{y}, \quad \mathbf{x} \in \mathcal{R}^n, \mathbf{y} \in \mathcal{R}^m, \quad (\text{D1})$$

which depends on *many* parameters Θ . We employ a feedforward neural network, specifically a multi-layer perceptron (MLP) with three hidden layers in addition to the input and output layers. The detailed architecture is presented in Table II.

A fundamental aspect of supervised learning is the requirement of a labeled dataset for neural network training¹⁷⁶². This includes pairs $(\mathbf{x}_i, \hat{\mathbf{y}}_i)_{i=1,2,\dots,N}$, where each input vector \mathbf{x}_i has an associated output vector $\hat{\mathbf{y}}_i$. The output from any given layer (l) is represented as a vector $\mathbf{y}^{(l)}$, where each component of this vector corresponds to the output generated by the neurons in that layer

$$\mathbf{y}^{(l)} = f^{(l)}(\mathbf{z}^{(l)}), \quad (\text{D2})$$

where, $f^{(l)}$ denotes a nonlinear function known as the *activation function*^{49,63}, and

$$\mathbf{z}^{(l)} = \mathbf{w}^{(l)} \mathbf{y}^{(l-1)} + \mathbf{b}^{(l)}. \quad (\text{D3})$$

Here, $\mathbf{w}^{(l)} \in \mathbb{R}^{D^{(l)} \times D^{(l-1)}}$ is the weight matrix, $\mathbf{b}^{(l)} \in \mathbb{R}^{D^{(l)}}$ is the bias vector, $D^{(l)}$ represents the dimension or number of neurons in l -th layer. Training the model begins by randomly initializing the weights and biases, and then proceeds by updating them using a variation of *stochastic gradient descent*, in particular we used the *adam* optimizer^{64,65}. This process stops when the cost function $C(\{\mathbf{y}_i, \hat{\mathbf{y}}_i\}_i)$ is minimized. We have opted for *Sparse Categorical Crossentropy*⁴⁹ as our cost function as mentioned in the main text. Although both *Categorical Crossentropy*⁴⁶ and *Sparse Categorical Crossentropy* share the same functional structure, the latter offers benefits due to its use of integer labeling. This approach requires less memory and computations, unlike *Categorical Crossentropy*, which necessitates one-hot encoding^{46,47} for the labels.

As shown in Table II, the implementation includes *leaky rectified linear unit* (LeakyReLU)⁵⁰ for the hidden layers as the activation function to prevent the ‘dying ReLU’ issue⁵⁰ and achieve superior outcomes. The function is defined as:

$$f_{\text{LReLU}}(z) = \begin{cases} z & \text{if } z \geq 0, \\ \alpha z & \text{if } z < 0, \end{cases} \quad (\text{D4})$$

where α is set to 0.01. In the output layer, the *Softmax* activation^{47,66} function was employed to ensure that the resulting output from each neuron span from 0 to 1 and adds up to 1. These values indicate the probabilities that the noise affecting the qubit falls into one of the 6 categories

$$\mathbf{y} = f_{\text{softmax}}(\mathbf{z}^{(L)}) = \frac{e^{\mathbf{z}^{(L)}}}{\sum_{k=1}^{D^{(L)}} e^{z_k^{(L)}}}, \quad (\text{D5})$$

where the exponentiation and division are performed element-wise.

AUTHORS DECLARATIONS

The authors have no conflicts to disclose.

ACKNOWLEDGMENTS

GF and LG acknowledge support from the PNRR MUR project PE0000023-NQSTI “National Quantum Science and Technology Institute”; SM acknowledge support from the ICSC - Centro Nazionale di Ricerca in High-Performance Computing, Big Data and Quantum Computing; GF acknowledges support from PRIN 2022 “SuperNISQ”; GF and EP acknowledge support from the University of Catania, Piano Incentivi Ricerca di Ateneo 2024-26, project QTCM; MP acknowledges funding from the Royal Society Wolfson Fellowship (RSWF/R3/183013), the Department for the Economy of Northern Ireland under the US-Ireland R&D Partnership Programme, and the EU Horizon Europe EIC Pathfinder project QuCoM (GA no. 10032223). EP acknowledges the COST Action SUPERQUMAP (CA 21144).

- ¹C. P. Koch, U. Boscain, T. Calarco, G. Dirr, S. Filipp, S. J. Glaser, R. Kosloff, S. Montangero, T. Schulte-Herbrüggen, D. Sugny, and F. K. Wilhelm, “Quantum optimal control in quantum technologies. Strategic report on current status, visions and goals for research in Europe,” *EPJ Quantum Technol.* **9**, 19 (2022).
- ²A. Acín, I. Bloch, H. Buhrman, T. Calarco, C. Eichler, J. Eisert, D. Esteve, N. Gisin, S. J. Glaser, F. Jelezko, S. Kuhr, M. Lewenstein, M. F. Riedel, P. O. Schmidt, R. Thew, A. Wallraff, I. Walmsley, and F. K. Wilhelm, “The quantum technologies roadmap: A European community view,” *New J. Phys.* **20**, 080201 (2018).
- ³W. H. Zurek, “Decoherence, einselection, and the quantum origins of the classical,” *Rev. Mod. Phys.* **75**, 715–775 (2003).
- ⁴H. M. Lim, G. T. Genov, R. Sailer, A. Fahrurrachman, M. A. Majidi, F. Jelezko, and R. S. Said, “Efficiency of optimal control for noisy spin qubits in diamond,” *Phys. Rev. Appl.* **24**, 054064 (2025).
- ⁵M. Kjaergaard, M. E. Schwartz, J. Braumüller, P. Krantz, J. I.-J. Wang, S. Gustavsson, and W. D. Oliver, “Superconducting Qubits: Current State of Play,” *Annu. Rev. Condens. Matter Phys.* **11**, 369–395 (2020).
- ⁶L. Postler, F. Butt, I. Pogorelov, C. D. Marciniak, S. Heußen, R. Blatt, P. Schindler, M. Rispler, M. Müller, and T. Monz, “Demonstration of Fault-Tolerant Steane Quantum Error Correction,” *PRX Quantum* **5**, 030326 (2024).
- ⁷D. Maile and J. Ankerhold, “Performance of quantum registers in diamond in the presence of spin impurities,” *Phys. Rev. B* **110**, 035407 (2024).
- ⁸G. Falci, M. Berritta, A. Russo, A. D’Arrigo, and E. Paladino, “Effects of low-frequency noise in driven coherent nanodevices,” *Phys. Scr.* **T151**, 014020 (2012).
- ⁹U. von Lüpke, F. Beaudoin, L. M. Norris, Y. Sung, R. Winik, J. Y. Qiu, M. Kjaergaard, D. Kim, J. Yoder, S. Gustavsson, L. Viola, and W. D. Oliver, “Two-Qubit Spectroscopy of Spatiotemporally Correlated Quantum Noise in Superconducting Qubits,” *PRX Quantum* **1**, 010305 (2020).
- ¹⁰J. M. Boter, X. Xue, T. Krähenmann, T. F. Watson, V. N. Premakumar, D. R. Ward, D. E. Savage, M. G. Lagally, M. Friesen, S. N. Coppersmith, M. A. Eriksson, R. Joynt, and L. M. K. Vandersypen, “Spatial noise correlations in a Si/SiGe two-qubit device from Bell state coherences,” *Phys. Rev. B* **101**, 235133 (2020).
- ¹¹J. Zou, S. Bosco, and D. Loss, “Spatially correlated classical and quantum noise in driven qubits: The good, the bad, and the ugly,” (2023), arXiv:2308.03054 [cond-mat, physics:quant-ph].
- ¹²J. Rojas-Arias, A. Noiri, P. Stano, T. Nakajima, J. Yoneda, K. Takeda, T. Kobayashi, A. Sammak, G. Scappucci, D. Loss, and S. Tarucha, “Spatial noise correlations beyond nearest neighbors in ${}^{\sim}{}^{28}\text{Si}/\text{Si-Ge}$ spin qubits,” *Phys. Rev. Appl.* **20**, 054024 (2023).
- ¹³J. Yoneda, J. S. Rojas-Arias, P. Stano, K. Takeda, A. Noiri, T. Nakajima, D. Loss, and S. Tarucha, “Noise-correlation spectrum for a pair of spin qubits in silicon,” *Nat. Phys.* , 1–6 (2023).
- ¹⁴A. B. Zorin, F.-J. Ahlers, J. Niemeyer, T. Weimann, H. Wolf, V. A. Krupenin, and S. V. Lotkhov, “Background charge noise in metallic single-electron tunneling devices,” *Phys. Rev. B* **53**, 13682–13687 (1996).
- ¹⁵A. P. Vepsäläinen, A. H. Karamlou, J. L. Orrell, A. S. Dogra, B. Loer, F. Vasconcelos, D. K. Kim, A. J. Melville, B. M. Niedzielski, J. L. Yoder, S. Gustavsson, J. A. Formaggio, B. A. VanDevender, and W. D. Oliver, “Impact of ionizing radiation on superconducting qubit coherence,” *Nature* **584**, 551–556 (2020).
- ¹⁶A. D’Arrigo, G. Piccitto, G. Falci, and E. Paladino, “Open-loop quantum control of small-size networks for high-order cumulants and cross-correlations sensing,” *Sci Rep* **14** (2024), 10.1038/s41598-024-67503-x, publisher: Nature Publishing Group.
- ¹⁷F. Marquardt, “Machine learning and quantum devices,” *SciPost Physics Lecture Notes* , 029 (2021).
- ¹⁸M. Krenn, J. Landgraf, T. Foesel, and F. Marquardt, “Artificial intelligence and machine learning for quantum technologies,” *Phys. Rev. A* **107**, 010101 (2023).
- ¹⁹V. Gebhart, R. Santagati, A. A. Gentile, E. M. Gauger, D. Craig, N. Ares, L. Banchi, F. Marquardt, L. Pezzè, and C. Bonato, “Learning quantum systems,” *Nat Rev Phys* , 1–16 (2023).
- ²⁰J. Brown, P. Sgroi, L. Giannelli, G. S. Paraoanu, E. Paladino, G. Falci, M. Paternostro, and A. Ferraro, “Reinforcement learning-enhanced protocols for coherent population-transfer in three-level quantum systems,” *New J. Phys.* **23**, 093035 (2021).
- ²¹L. Giannelli, S. Sgroi, J. Brown, G. S. Paraoanu, M. Paternostro, E. Paladino, and G. Falci, “A tutorial on optimal control and reinforcement learning methods for quantum technologies,” *Physics Letters A* **434**, 128054 (2022).
- ²²M. Y. Niu, S. Boixo, V. N. Smelyanskiy, and H. Neven, “Universal quantum control through deep reinforcement learning,” *npj Quantum Inf* **5**, 1–8 (2019).
- ²³P. Sgroi, G. M. Palma, and M. Paternostro, “Reinforcement learning approach to nonequilibrium quantum thermodynamics,” *Physical Review Letters* **126**, 020601 (2021).
- ²⁴L. Banchi, E. Grant, A. Rocchetto, and S. Severini, “Modelling non-markovian quantum processes with recurrent neural networks,” *New J. Phys.* **20**, 123030 (2018).
- ²⁵G. Torlai, G. Mazzola, J. Carrasquilla, M. Troyer, R. Melko, and G. Carleo, “Neural-network quantum state tomography,” *Nature Phys* **14**, 447–450 (2018).
- ²⁶A. M. Palmieri, E. Kovlakov, F. Bianchi, D. Yudin, S. Straupe, J. D. Biamonte, and S. Kulik, “Experimental neural network enhanced quantum tomography,” *npj Quantum Inf* **6**, 1–5 (2020).
- ²⁷J. Barr, G. Zicari, A. Ferraro, and M. Paternostro, “Spectral density classification for environment spectroscopy,” *Machine Learning: Science and Technology* **5**, 015043 (2024).
- ²⁸J. Barr, A. Ferraro, M. Paternostro, and G. Zicari, “Machine learning-enhanced characterisation of structured spectral densities: Leveraging the reaction coordinate mapping,” arXiv preprint arXiv:2501.07485 (2025).
- ²⁹J. Barr, S. Mukherjee, A. Ferraro, M. Paternostro, and G. Zicari, “A machine learning based approach to the identification of spectral densities in quantum open systems,” arXiv preprint arXiv:2507.13730 (2025).

- ³⁰S. Mukherjee, D. Penna, F. Cirinnà, M. Paternostro, E. Paladino, G. Falci, and L. Giannelli, “Noise classification in three-level quantum networks by Machine Learning,” *Mach. Learn.: Sci. Technol.* **5**, 045049 (2024).
- ³¹S. Martina, S. Gherardini, and F. Caruso, “Machine learning classification of non-Markovian noise disturbing quantum dynamics,” *Phys. Scr.* **98**, 035104 (2023).
- ³²J. Preskill, “Quantum Computing in the NISQ era and beyond,” *Quantum* **2**, 79 (2018).
- ³³K. Bergmann, H. Theuer, and B. W. Shore, “Coherent population transfer among quantum states of atoms and molecules,” *Rev. Mod. Phys.* **70**, 1003–1025 (1998).
- ³⁴N. V. Vitanov, A. A. Rangelov, B. W. Shore, and K. Bergmann, “Stimulated Raman adiabatic passage in physics, chemistry, and beyond,” *Rev. Mod. Phys.* **89**, 015006 (2017).
- ³⁵J. Siewert, T. Brandes, and G. Falci, “Adiabatic passage with superconducting nanocircuits,” *Optics Communications Quantum Control of Light and Matter*, **264**, 435–440 (2006).
- ³⁶J. Siewert, T. Brandes, and G. Falci, “Advanced control with a Cooper-pair box: Stimulated Raman adiabatic passage and Fock-state generation in a nanomechanical resonator,” *Phys. Rev. B* **79**, 024504 (2009).
- ³⁷G. Falci, A. La Cognata, M. Berritta, A. D’Arrigo, E. Paladino, and B. Spagnolo, “Design of a Lambda system for population transfer in superconducting nanocircuits,” *Phys. Rev. B* **87**, 214515 (2013).
- ³⁸G. Falci, P. G. Di Stefano, A. Ridolfo, A. D’Arrigo, G. S. Paraoanu, and E. Paladino, “Advances in quantum control of three-level superconducting circuit architectures,” *Fortschritte der Physik* **65**, 1600077 (2017).
- ³⁹K. S. Kumar, A. Vepsäläinen, S. Danilin, and G. S. Paraoanu, “Stimulated Raman adiabatic passage in a three-level superconducting circuit,” *Nat Commun* **7**, 10628 (2016).
- ⁴⁰H. K. Xu, C. Song, W. Y. Liu, G. M. Xue, F. F. Su, H. Deng, Y. Tian, D. N. Zheng, S. Han, Y. P. Zhong, H. Wang, Y.-x. Liu, and S. P. Zhao, “Coherent population transfer between uncoupled or weakly coupled states in ladder-type superconducting qutrits,” *Nat Commun* **7**, 11018 (2016).
- ⁴¹L. Mandel and E. Wolf, *Optical Coherence and Quantum Optics* (Cambridge ; New York, 1995).
- ⁴²E. Paladino, Y. M. Galperin, G. Falci, and B. L. Altshuler, “ $\$1/f\$$ noise: Implications for solid-state quantum information,” *Rev. Mod. Phys.* **86**, 361–418 (2014).
- ⁴³E. Paladino, L. Faoro, G. Falci, and R. Fazio, “Decoherence and $1/f$ noise in Josephson qubits,” *Phys. Rev. Lett.* **88**, 228304 (2002).
- ⁴⁴G. Falci, A. D’Arrigo, A. Mastellone, and E. Paladino, “Initial decoherence in solid state qubits,” *Phys. Rev. Lett.* **94**, 167002 (2005).
- ⁴⁵F. Otterpohl, P. Nalbach, E. Paladino, G. A. Falci, and M. Thorwart, “Quantum $1/f^n$ noise induced relaxation in the spin-boson model,” (2025), arXiv:2507.14329 [quant-ph].
- ⁴⁶I. Goodfellow, Y. Bengio, and A. Courville, *Deep Learning, Adaptive Computation and Machine Learning* (Cambridge, Massachusetts, 2016).
- ⁴⁷C. M. Bishop and N. M. Nasrabadi, *Pattern recognition and machine learning*, Vol. 4 (Springer, 2006).
- ⁴⁸K. Hornik, M. Stinchcombe, and H. White, “Multilayer feedforward networks are universal approximators,” *Neural Networks* **2**, 359–366 (1989).
- ⁴⁹A. Géron, *Hands-on Machine Learning with Scikit-Learn, Keras, and TensorFlow: Concepts, Tools, and Techniques to Build Intelligent Systems*, third edition ed. (Beijing Boston Farnham Sebastopol Tokyo, 2023).
- ⁵⁰X. Glorot, A. Bordes, and Y. Bengio, “Deep sparse rectifier neural networks,” in *Proceedings of the fourteenth international conference on artificial intelligence and statistics (JMLR Workshop and Conference Proceedings, 2011)* pp. 315–323.
- ⁵¹P. G. Di Stefano, E. Paladino, A. D’Arrigo, and G. Falci, “Population transfer in a Lambda system induced by detunings,” *Phys. Rev. B* **91**, 224506 (2015).
- ⁵²P. G. Di Stefano, E. Paladino, T. J. Pope, and G. Falci, “Coherent manipulation of noise-protected superconducting artificial atoms in the Lambda scheme,” *Phys. Rev. A* **93**, 051801 (2016).
- ⁵³J. Brown, S. Sgroi, L. Giannelli, G. S. Paraoanu, E. Paladino, G. Falci, M. Paternostro, and A. Ferraro, “Reinforcement learning-enhanced protocols for coherent population-transfer in three-level quantum systems,” *New J. Phys.* **23**, 093035 (2021).
- ⁵⁴P. G. Di Stefano, J. J. Alonso, E. Lutz, G. Falci, and M. Paternostro, “Nonequilibrium thermodynamics of continuously measured quantum systems: A circuit QED implementation,” *Phys. Rev. B* **98**, 144514 (2018).
- ⁵⁵L. Giannelli, E. Paladino, M. Grajcar, G. S. Paraoanu, and G. Falci, “Detecting virtual photons in ultrastrongly coupled superconducting quantum circuits,” *Phys. Rev. Res.* **6**, 013008 (2024).
- ⁵⁶L. Giannelli, G. Anfuso, M. Grajcar, G. S. Paraoanu, E. Paladino, and G. Falci, “Integrated conversion and photodetection of virtual photons in an ultrastrongly coupled superconducting quantum circuit,” *Eur. Phys. J. Spec. Top.* **232**, 3387–3392 (2023).
- ⁵⁷B. Shore, “The Theory of Coherent Atomic Excitation,” *Fusion Technology* **19**, 576–577 (1991).
- ⁵⁸M. Born and V. Fock, “Beweis des adiabatenatzes,” *Zeitschrift für Physik* **51**, 165–180 (1928).
- ⁵⁹A. Messiah, *Quantum Mechanics, Vol. 1/2* (1961).
- ⁶⁰L. Giannelli and E. Arimondo, “Three-level superadiabatic quantum driving,” *Phys. Rev. A* **89**, 033419 (2014).
- ⁶¹F. Marquardt, “Machine learning and quantum devices,” *SciPost Physics Lecture Notes*, 029 (2021).
- ⁶²R. F. AI, “Hands-On Machine Learning with Scikit-Learn, Keras, and TensorFlow 2nd Edition PDF,” (2018).
- ⁶³S. Haykin, *Neural networks and learning machines, 3/E* (Pearson Education India, 2009).
- ⁶⁴D. P. Kingma, “Adam: A method for stochastic optimization,” arXiv preprint arXiv:1412.6980 (2014).
- ⁶⁵D. P. Kingma and J. Ba, “Adam: A method for stochastic optimization,” 3rd International Conference on Learning Representations, Conference Track Proceedings (2015).
- ⁶⁶D. J. MacKay, *Information theory, inference and learning algorithms* (Cambridge university press, 2003).